



**One-Phonon sideband and multiphonon relaxation in
La_{1.6}Mo₂O₉: Eu^{0.43+} and β-NaGdF₄:Tb³⁺ nanocrystals**

Journal:	<i>RSC Advances</i>
Manuscript ID:	RA-ART-01-2015-000912
Article Type:	Paper
Date Submitted by the Author:	16-Jan-2015
Complete List of Authors:	Liu, Chunxu; Changchun Institute of Optics, Fine Mechanics and Physics, Key Laboratory of Luminescence and Applications Zhang, Jisen; Changchun Institute of Optics, Fine Mechanics and Physics, Luo, Yongshi; Changchun Institute of Optics, Fine Mechanics and Physics,

One-phonon sideband and multiphonon relaxation in $\text{La}_{1.6}\text{Mo}_2\text{O}_9$: $\text{Eu}_{0.4}^{3+}$ and $\beta\text{-NaGdF}_4\text{:Tb}^{3+}$ nanocrystals

Chunxu Liu, Jisen Zhang, and Yongshi Luo

State Key Laboratory of Luminescence and Applications, Changchun Institute of Optics, Fine Mechanics and

Physics, Chinese Academy of Sciences, Changchun 130033, P. R. China

The experimental studies of one-phonon sideband (PSB) and multiphonon relaxation (MR) involving a large energy gap (5800 cm^{-1}) crossover from bulk to nanocrystal (NC) system were reported. Two one-phonon sidebands, $\text{PSB}_1=449\text{ nm}$ and $\text{PSB}_2=429\text{ nm}$ associated with the Eu^{3+} ${}^7\text{F}_0\rightarrow{}^5\text{D}_2$ 464 nm zero phonon line (ZPL) were observed in the excitation spectra monitoring Eu^{3+} ${}^5\text{D}_0\rightarrow{}^7\text{F}_2$ 613 nm, resulted from Mo-O and O-Mo-O local mode vibrations, respectively. The phonon density of states of $\rho(\omega)$ were determined from the profile of PSB. The temperature dependence of MR rate for the Tb^{3+} ${}^5\text{D}_3\rightarrow{}^5\text{D}_4$ of in $\beta\text{-NaGdF}_4\text{:Tb}^{3+}$ NCs was analyzed in a single-frequency approximation of phonon spectrum in the framework of the nonlinear theory of MR. The experimental data were well agreed with the theoretical curves within the range of 12K to 312K. It is concluded that the MR occurs predominantly via high-energy optical phonons.

Introduction

It is well known that phonons play an important role in luminescence spectroscopy, excited state relaxation and energy-transfer processes.¹⁻⁵ Furthermore, experimental results and subsequent analysis on the relaxation dynamics between various excited levels of rare-earth (RE) ions suggest that two different groups as regards spatial localization, i.e., one of them represents phonons of the normal unperturbed lattice and the other is a localized mode involved in the process. There is a large difference between the local electron states and the electron states of the free atoms. The interactions between the local electron states and around atoms in the sites of lattice result in more or less the shift of equilibration position of atoms, or the local electron states lead to the distort of lattices which is so-called lattice relaxation.

The electron-phonon interaction arises because the full wave function of the system depends on the positions of the electrons and the ions. When an electronic transition occurs, we have a change in the equilibrium position of the ions around the impurity and this is expressed by an interaction between electrons and ions. In the case of weak electron-phonon interaction, i.e. at small Huang-Rhys factor S ($S \leq 1$), one observes in the spectrum the intense zero phonon line (ZPL) and the accompanying weak phonon sideband associated mainly with one-phonon transitions. At large S ($S > 5$)⁶, i.e. in the case of strong electron-phonon interaction, the intensity of the ZPL is very small and one observes in the spectrum only a broad phonon band associated with the multiphonon transitions. Based on the single-configuration-coordinate (SCC) model⁷⁻¹⁰, the profile of the phonon sideband (PSB) were analyzed by Jia, Brundage and Yen¹⁰ in the strong electron-phonon interaction case ($S=9.5$ and 9.7). Up to now, a few papers have been published on investigation of the one phonon sideband in the weak electron-phonon interaction case ($S < 1$)¹¹ and with little attention on the relation between the profile $I(\omega)$ of the phonon sideband and phonon density of states $\rho(\omega)$.

The 4f orbitals of the rare earth ion are hardly bonding, and they lie within the energy gap. Furthermore,

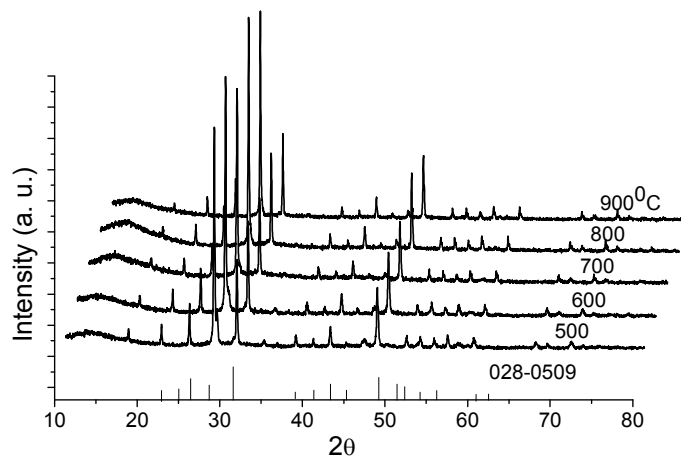


Fig. 1 XRD patterns of La₂Mo₂O₉:Eu³⁺.

because the rare earth 4f orbitals are shielded by the outer 5s² and 5p⁶ orbitals, they are hardly affected by the ligand belong to the weak interaction case. Since a widespread applications (such as lighting and display etc.) rest on the interaction between the 4f electrons and the surroundings, it is justified to investigate the vibronic transitions of the rare earth ions.

The ultraviolet (UV) emission from a GaN-based light emitting diode (LED) can be absorbed by the Mo-O charge transfer bands in molybdates very efficiently. When doping Eu³⁺ in the molybdates, the excitation energy can be transferred to the activator ions Eu³⁺ nonradiatively, resulting in the red emission of Eu³⁺.¹²⁻¹⁴ In recent years, molybdate compounds have gained much attention due to their negative thermal expansion (NTE) property.¹⁵⁻¹⁷ The facile synthesis and chemical stability make the molybdate good dopant host.

The serial samples (d=4.7, 56.0 and 115.5 nm) of β-NaGdF₄ were synthesized. As for the β-phase NaGdF₄, there are three different cation sites in the lattice, i.e., 1a, 1f, and 2h, among which 2h sites are normally occupied by only sodium ions, 1a and 1f sites are occupied by Ln³⁺ ions. The β-phase is more ordered and thermodynamically stable. The β-phase NaGdF₄ is more suitable as a matrix of down and up conversion material. The energy gap below ⁵D₄ of Tb³⁺ was so large (~15000 cm⁻¹) that multiphonon emission relaxation can be

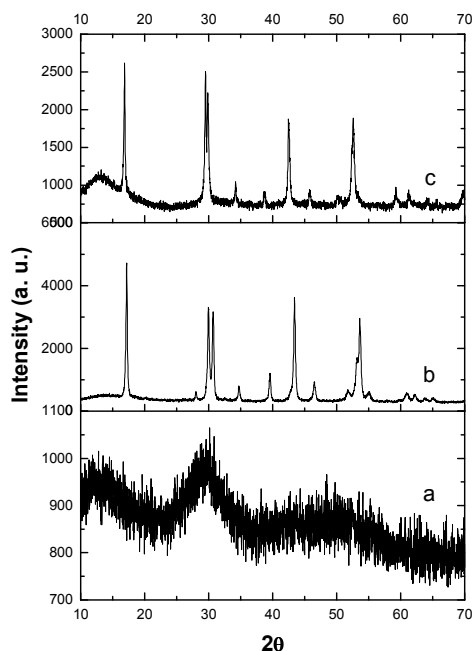


Fig. 2 XRD patterns of β -NaGdF₄:Tb³⁺ nanocrystals.

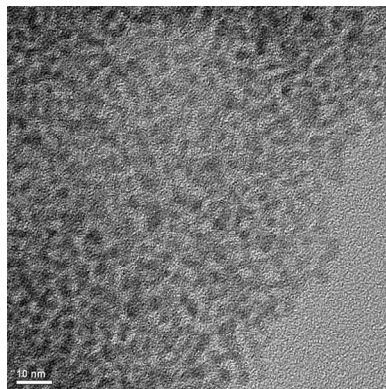
neglected.

In this paper, by increasing the dopant concentration of Eu³⁺ (up to 20 mol %) and component of (NH₄)₆Mo₇O₂₄ · 4H₂O (exceed the stoichiometric ratio 30 %) in the synthesis, two one-phonon sidebands PSB₁=449 nm and PSB₂=429 nm associated with the Eu³⁺ ⁷F₀→⁵D₂ excitation transition at 464 nm (ZPL) were observed in the excitation spectra monitoring the Eu³⁺ ⁵D₀→⁷F₂ emission at 613 nm. The average phonon energy involved in the sideband formation are $\hbar\omega_{L1}$ =612 cm⁻¹ and $\hbar\omega_{L2}$ =1077 cm⁻¹, respectively. Furthermore, the phonon density of states $\rho(\omega)$ was determined experimentally from the profile of one-phonon sideband. It is important to study the phonon-impurity and phonon-phonon interactions.

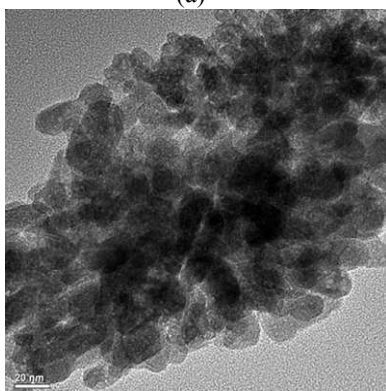
Experiment section

Materials

In combustion synthesis of La_{1.6}Mo₂O₉: Eu_{0.4}³⁺, La₂O₃ (99.99%), Eu₂O₃ (99.99%), (NH₄)₆Mo₇O₂₄ · 4H₂O (AR)



(a)



(b)

Fig. 3 TEM pictures of β -NaGdF₄:Tb³⁺ nanocrystals, (a) d=4.7 nm; (b) d=56.0 nm.

and citric acid (AR) as well in the preparation of β -NaGdF₄:Tb³⁺ nanocrystals by hydrothermal method, Gd(NO₃)₃ · 6H₂O, NaCl, Tb(NO₃)₃ · 7H₂O, Er(NO₃)₃ · 5H₂O, Gd(NO₃)₃ · 6H₂O, and Tb(NO₃)₃ · 7H₂O were all used as received without additional purification or treatment.

Synthesis

A powder of 20 mol % Eu³⁺ ion-doped rare earth molybdates La₂Mo₂O₉:Eu was prepared by using the combustion method.¹⁸ According to the stoichiometric ratio, 1.96×10^{-2} mol La₂O₃ (99.99 %), and 0.4×10^{-2} mol Eu₂O₃ (99.99 %) HNO₃ (analytical reagent, AR) under vigorous stirring, and the pH value of the solution was adjusted

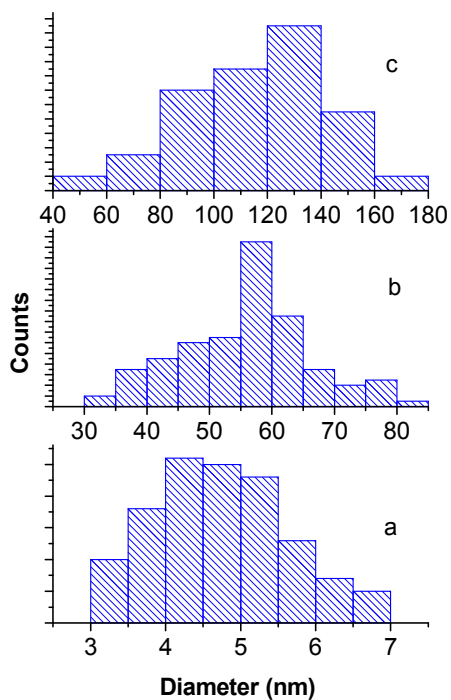


Fig. 4 Histograms of (a) sample a ($d=4.7\text{nm}$); (b) sample b ($d=56.0\text{nm}$) and (c) sample c ($d=115.5\text{nm}$).

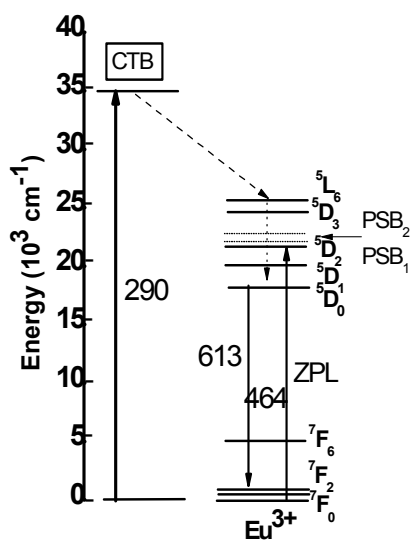


Fig. 5 Energy level and mechanism scheme depicting the PSB process of $\text{La}_2\text{Mo}_2\text{O}_9:\text{Eu}$.

completely, the mixing materials were combusted at a moment, and the white powders were obtained. The

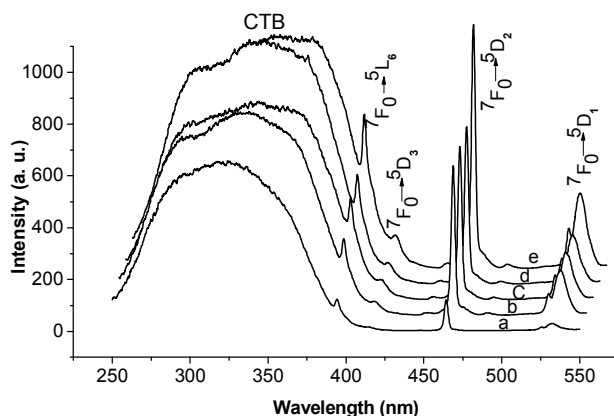


Fig. 6 Excitation spectra monitoring the $\text{Eu}^{3+} \ ^5\text{D}_2 \rightarrow \ ^7\text{F}_0$ emission at 613 nm, a-e lines corresponding the annealing temperatures at 500, 600, 700, 800 and 900 °C, respectively.

to 2-3 by dilute $\text{NH}_3 \cdot \text{H}_2\text{O}$. Then, 0.29×10^{-2} mol $(\text{NH}_4)_6\text{Mo}_7\text{O}_{24} \cdot 4\text{H}_2\text{O}$ (AR) as well as 30 mL of a water-ethanol solution (volume ratio of water and ethanol is 1:8) of citric acid (AR) were added to the solution. The molar ratio of metal ions to citric acid was 1:2. The mixing solution was heated on electric Oven. After water was evaporated products were annealed at 500-900 °C different temperatures for 2 h in air to get the final products.

The serial samples of $\beta\text{-NaGdF}_4: \text{Tb}^{3+}$ 1% mol NCs were prepared by hydrothermal method with Span 80 template. A total of 30 mL of 1-butanol, 20 mL of water, and 4.5 mL of Span 80 were mixed and stirred for 10 min. This solution was divided into two parts. In one part, a solution mixture of 0.42 M of $\text{Gd}(\text{NO}_3)_3 \cdot 6\text{H}_2\text{O}$, and 0.42 M of NaCl, and the required amount of $\text{Tb}(\text{NO}_3)_3 \cdot 7\text{H}_2\text{O}$ and $\text{Er}(\text{NO}_3)_3 \cdot 5\text{H}_2\text{O}$ were added and stirred for 10 min. A 1.7 M solution of NH_4F was added to another part of the solution and stirred for 5 min. Finally, the two solutions were mixed and this mixture was put into a Teflon-lined stainless steel autoclave and maintained at 170 °C for 2 h. In this preparation technique, $\text{Ln}^{3+}/\text{F}^-$ ratio and pH were maintained at 1:4 and 6:7 respectively. The NC sizes of $\beta\text{-NaGdF}_4: \text{Tb}^{3+}$ were controlled by the synthesizing temperatures (170 °C), concentrations (1.7-3.4 M) and pH values (5-7) with NaOH.

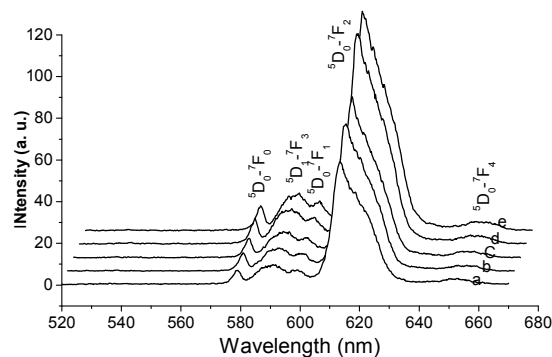


Fig. 7 Emission spectra of $\text{La}_2\text{Mo}_2\text{O}_9:\text{Eu}^{3+}$ under excitation at 290 nm in CTB, a-e lines corresponding the annealing temperatures at 500, 600, 700, 800 and 900 °C, respectively.

Apparatus

Powder X-ray diffraction (XRD) measurements were carried out by using a Bruker D8 advanced powder diffractometer with Cu KR radiation ($\lambda=1.54056 \text{ \AA}$) as the incident beam. The patterns were collected at room temperature with a 2θ range of 10° - 80° for $\text{La}_2\text{Mo}_2\text{O}_9:20\%$ mol Eu and 10° - 70° for $\beta\text{-NaGdF}_4:\text{Tb}^{3+}$ 1 % mol. The morphology and particle size of the final products were characterized with a TEM (Technai T12). A sunlight (optical parametric oscillator, OPO) laser was used as the exciting source. A TDS 3052 digital phosphor oscilloscope was used to record the luminescence decay curves. The lifetime measurements were performed monitoring Tb^{3+} emission at 383 nm ($^5\text{D}_3 \rightarrow ^7\text{F}_6$) excited by 273 nm ($\text{Gd}^{3+} \text{ } ^8\text{S}_{7/2} \rightarrow ^6\text{I}_J$). The decay signals were processed by a Boxcar Averager (Model 162).

The excitation spectra were performed on a Hitachi F-7000 fluorescence spectrophotometer equipped with a 150 W xenon lamp as the excitation light source. The scan speed is 240 nm min^{-1} , and the slit width is 1.0 nm.

Results and discussions

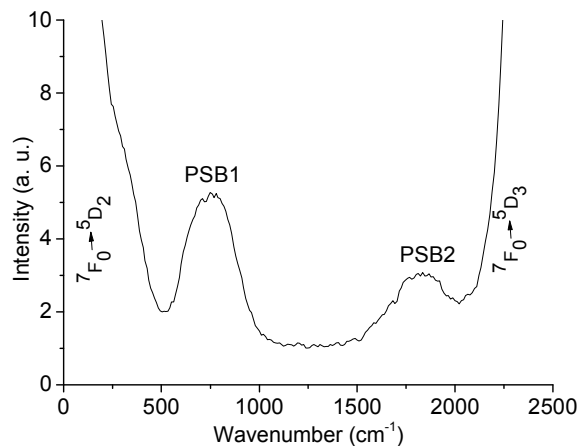


Fig. 8 Excitation spectrum monitoring the $\text{Eu}^{3+} \ ^5\text{D}_2 \rightarrow \ ^7\text{F}_0$ emission at 613 nm, is a part of e-line in the Fig. 6.

Characterization and measurements

From the powder XRD patterns (Fig. 1), we can find that the $\text{La}_2\text{Mo}_2\text{O}_9:\text{Eu}$ phosphors are pure phase and well-crystallized. $\text{La}_2\text{Mo}_2\text{O}_9:\text{Eu}$ can be indexed to JCPDS 028-0509. No phase transition occurs though the annealing temperatures (500-900 °C), while with a decrease in annealing temperature, the profiles of the peaks broaden and the intensity diminishes. The XRD patterns of $\beta\text{-NaGdF}_4:\text{Tb}^{3+}$ was shown in Fig. 2. It is obvious that the widths of XRD-peaks are changed with the sizes of samples. For the accurate determination of size, the transperence electron microscope (TEM) measurements were performed (Fig. 3). The histograms derived from Fig. 3 were shown in Fig. 4. The average particle sizes were found to be $d=4.7, 56.0$ and 115.5 nm, which agreed with those obtained from the Scherrer's formula.

One-phonon sideband

The Eu^{3+} ion is the well known spectroscopic probe to estimate the local environment in various crystals and glasses due to its simple energy level structure that is the $\ ^7\text{F}_0$ ground and the $\ ^5\text{D}_0$ excited states of Eu^{3+} ion are singles and non-degenerate under any symmetry. The energy level diagram depicting the PSB process is shown in

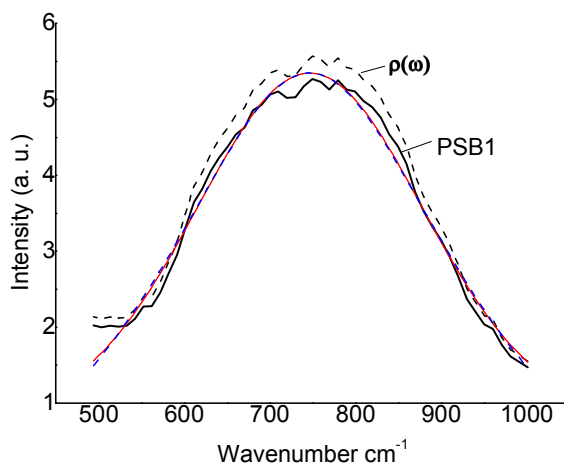


Fig. 9 The phonon density of states $\rho(\omega)$ and the fit curves by Gaussian (red line) and Lorentzian (blue-dashed line) line shapes of PSB1. The x-axis is the distance from the center (set as 0) of $\text{Eu}^{3+} {}^7\text{F}_0 \rightarrow {}^5\text{D}_2$ excitation peak.

Fig. 5. The excitation spectra (Fig. 6) were measured by monitoring the $\text{Eu}^{3+} {}^5\text{D}_2 \rightarrow {}^7\text{F}_0$ emission at 613nm. If the energy difference between bonding and antibonding orbitals of the Mo-O groups is equal to the energy of charge transfer band of the Eu^{3+} ions, the energy can be transferred from Mo-O groups through the charge transfer state to the 4f energy levels of Eu^{3+} ions nonradiatively. From the emission spectra under excitation 290 nm, see Fig. 7, we have been observed the energy transfer from Mo-O to the 4f energy levels of Eu^{3+} ions.

The theory of transition of multiphonon and relaxation of lattice was found in the following approximation:¹⁻¹⁷

- 1) A single frequency approximation or both parabolas of initial and final states have the same phonon energy $\hbar\omega$.
- 2) In the Golden Rule integration over the z coordinate, the Condon approximation is used.
- 3) The transition taken Place with the vibrational states of the initial parabola in thermal equilibrium with the host.

The Huang-Rhys-Pekar $W_p(S, \langle m \rangle)$ function is given by

$$W_p(S, \langle m \rangle) = e^{-S\langle 1+2m \rangle} \sum_{j=\max(0, -p)} \frac{(S\langle m \rangle)^j (S\langle 1+m \rangle)^{p+j}}{(p+j)! j!} \quad (1)$$

Where S is the Huang-Rhys factor, the parameter $\langle m \rangle = r/(1-r)$ is Planck's average thermal occupancy and $r =$

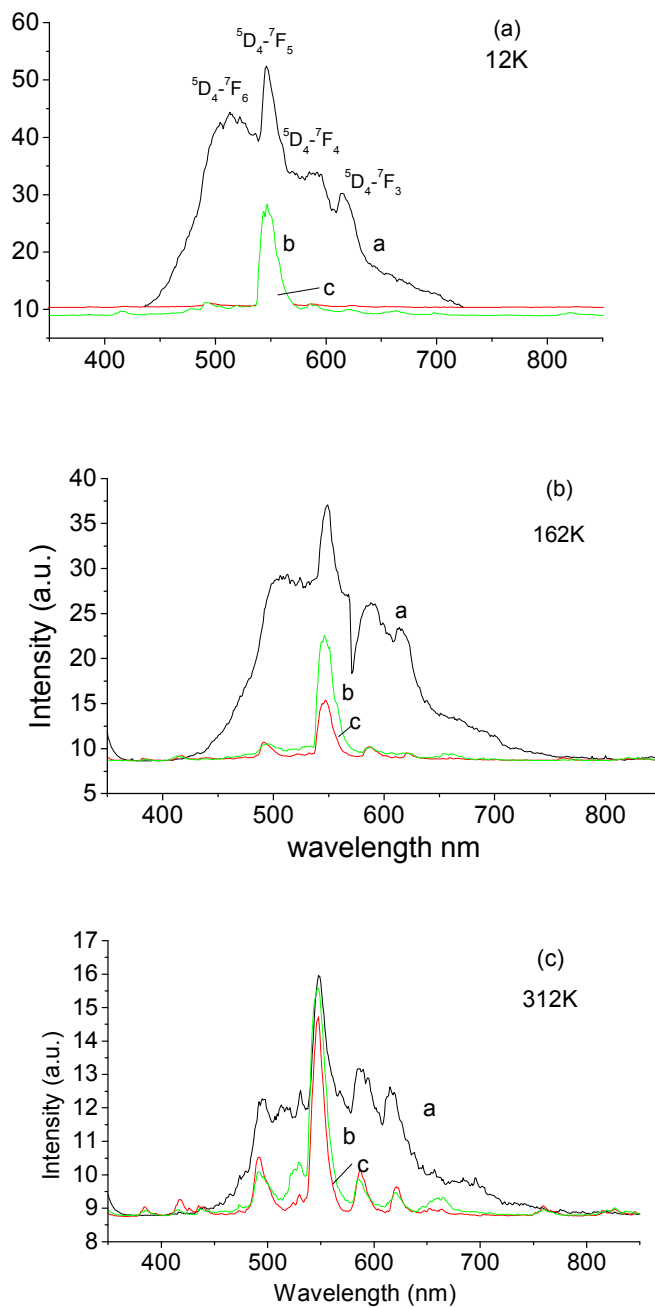


Fig. 10 Emission spectra of (a) sample a ($d=4.7\text{nm}$); (b) sample b ($d=56.0\text{nm}$) and (c) sample c ($d=115.5\text{nm}$)

excited by 273nm ($\text{Gd}^{3+} {}^8S_{7/2} - {}^6I_7$).

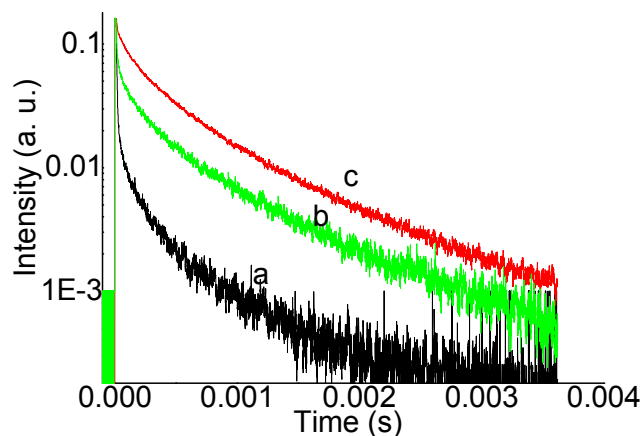


Fig. 11 Decay curves of $\text{Tb}^{3+} {}^5\text{D}_3\text{-}^7\text{F}_6$ transition (383nm) of samples a-c at $T=12\text{K}$.

$$S = \frac{I_{\text{PSB}}}{I_{\text{ZPL}}} = \frac{W_1(S, \langle m \rangle)}{W_0(S, \langle m \rangle)} = \begin{cases} S\langle 1+m \rangle; & P \geq 0; \\ S\langle m \rangle; & P < 0; \end{cases} \quad (2)$$

$\exp(-\hbar\omega/kT)$ is the normalized thermal weight of the initial vibrational state. In addition, the Huang-Rhys factor can be calculated according to eq. 2.

where I_{PSB} and I_{ZPL} are the integral intensity of PSB and ZPL, respectively. $P \geq 0$ is for the absorption of phonons, $p < 0$ is for the emission of phonons, respectively. Any radiative transition between electronic levels of an ion in a crystal, will exhibit emission and absorption sidebands due to the perturbation. These sidebands correspond to the simultaneous emission or absorption of phonons which occur due to the mixing of state functions via the perturbation. The ${}^7\text{F}_0 \rightarrow {}^5\text{D}_2$ 464 nm transition, namely, the ZLP, is a purely electric dipole transition according to transition selection rules shown in the Fig. 8 (a part of Fig. 6). Two one-phonon PSBs located at 449 and 429 nm at the high energy side of the ZPL were observed. They result from the simultaneous excitation of the electric transitions of Eu^{3+} and of vibrational modes around the dopant ion. The frequency gap Δ between the zero-phonon line and the peak of the phonon side band is determined by Franck-Condon principles. The two PSBs are due to the local mode arising from the Mo-O and O-Mo-O vibrations, respectively. This is a process of phonon absorption, therefore, $p \geq 0$ in eq. 2. In addition, $\langle 1+m \rangle$ can also be approximately set as 1 because of higher phonon energy at room temperature. Therefore, the Huang factor can also be expressed as the ratio of the integral

intensity of the one-phonon line and zero-phonon line $I_{\text{PSB}} / I_{\text{ZPL}}$ (see eq. (1)), then $S_1=0.055$ and $S_2=0.037$, respectively. It is indicated that when the strength of the electron-phonon coupling is weak ($S < 1$) we have an intense ZPL in the spectrum, on the contrary, when coupling is strong, the zero-phonon line is plunged in the multiphonon structure and cannot be separated. The profile of one-phonon PSB should be proportional both to the phonon density of states $\rho(\omega)$ and the probability of absorbing a phonon. An exact integrated relationship between the density of the phonon states and the shape of the phonon sideband in the general case of multiphonon transitions was obtained²¹

$$I(\omega, T) = \exp[-S(T)] \rho(\omega, T) + \frac{1}{\omega} \int_{-\infty}^{\infty} \rho(\omega, T) t I(\omega - t, T) dt, \quad (3)$$

where $I(\omega, T)$ is the function describing the shape of the phonon band. If one neglects the integral term corresponding to the multiphonon transitions, the shape of one-phonon sideband can be given

$$I_1(\omega) = \exp(-S) \rho(\omega). \quad (4)$$

With the S values above calculated, the phonon density of states $\rho(\omega)$ resulting from the impurity-phonon interaction can be determined and plotted in Fig. 9. It is shown that the profile of one-phonon PSB can be described well by both Gaussian and Lorentzian shapes in Fig. 9. The full width at half maximum (FWHM) of the profile phonon sideband can be given as $\text{FWHM} = 2[2 \ln 2 S (\hbar\omega_L)^2]^{1/2}$, from which the average energy of the phonons $\hbar\omega_L$ involved in the sideband formation can be derived, $\hbar\omega_{L1} = 612 \text{ cm}^{-1}$ and $\hbar\omega_{L2} = 1077 \text{ cm}^{-1}$, respectively.

MR of the $^5D_3 \rightarrow ^5D_4$ of Tb^{3+} in $\beta\text{-NaGdF}_4:\text{Tb}^{3+}$ NCs

Nonradiative transition is highly important in the study and design of devices of luminescence and lasing, because the competition between nonradiative transition and radiative transition decides the luminescence efficiency.

Materials doped with rare-earth ions are important in luminescence and lasing materials. Therefore nonradiative transition of rare-earth ions has attracted considerable attention. The radiative transition probability of rare-earth

ions (or intensity of spectral lines) can be calculated by applying the Judd-Ofelt theory.²²⁻²³ The theory of nonradiative transition of rare-earth ions has been investigated.²⁴⁻³¹ The linear theory of Miyakawa and Dexter predicts an exponential energy-gap law but is only valid for strong and intermediate electron-phonon coupling. A modified exponential energy-gap law reconciles the large variation in the exponential factor for transitions involving only a few phonons. The nonlinear theory of Pukhov and Sakun²⁶ is valid for weak electron-phonon coupling, harmonic lattice vibrations, and a single phonon frequency model. This theory also has the advantage of expressing the MR rates in terms of the reduced matrix elements $\langle J' \| U^{(k)} \| J \rangle$ from the Judd-Ofelt theory. The lack of theory adequately copes with the MR rates observed for transitions involving a large number of phonons ($n > 3$).³¹ To date, some phenomenological formulas are still applied to estimate nonradiative transition experiment. For lanthanide (Ln^{3+})-doped nanocrystals (NCs), confinement effects are induced mostly through electron-phonon interactions despite the localized 4f states. Thus, investigating the nonradiative transition, especially, MR of rare-earth ions involving large energy gaps is important. Any property of NCs that depends on the vibrational spectrum, such as its thermodynamic properties or electron-phonon dynamics, is different at low energies than in bulk crystals. This phenomenon is especially true for NCs, for example, only weak coupling occurred in their surroundings in powder form.

This section mainly investigated MR of NCs doped with rare-earth ions and compared it with that in the corresponding bulk material. The emission spectra excited by 273 nm ($\text{Gd}^{3+} \ ^8\text{S}_{7/2} \text{-}^6\text{I}_J$) and luminescence lifetimes of $^5\text{D}_3 \text{-}^7\text{F}_6$ transition of Tb^{3+} were measured at 12K to 312K, and MR rates for the $^5\text{D}_3 \rightarrow ^5\text{D}_4$ of Tb^{3+} in $\beta\text{-NaGdF}_4:\text{Tb}^{3+}$ NCs were calculated. The dependences on the temperature of MR rates for the $^5\text{D}_3 \rightarrow ^5\text{D}_4$ were analyzed by single-frequency approximation in the framework of the nonlinear theory of MR. The luminescent process in $\beta\text{-NaGdF}_4:\text{Tb}^{3+}$ started with excitation into the Gd^{3+} ion (273nm, $^8\text{S}_{7/2} \text{-}^6\text{I}_J$) 273 nm, and then energy migration among the inner lattices of Gd^{3+} occurred until the excitation energy was trapped by the activator ions Tb^{3+} from which emissions occurred. The emission spectra of samples were measured at seven temperatures ($T =$

12K to 312K). The emission spectra at 12K, 162K and 312K are given in Figures 10. The 5D_4 - \sum^7F_J ($J= 3, 4, 5, 6$) transitions were predominant in the emission spectra.

Temperature-dependent contributions to fluorescence lifetimes come from: (i) thermal population of nearby emitting levels (ii) vibrational 4f-5d and (iii) J-mixings as well as (iv) multiphonon emission processes. Because the energy gap between 5D_3 and 5D_4 is much larger than kT , the temperature variations of lifetimes of the 5D_3 - and 5D_4 -emissions are caused mainly by the first three processes. Therefore, the observed lifetimes showed relatively small and complicated temperature-variations. The luminescent decay curves of 5D_3 - 7F_6 transition (383nm) were fitted with the single exponential functions in Figure 11, and tabulated in Table1.

The multiphonon emission process of 5D_3 - 5D_4 sometimes became a dominant mode of decay of the 5D_3 state. The magnitude of static and vibrational crystal field acting on Tb^{3+} influenced the degree of the 4f-5d mixing and J-mixing, as well as the radiationless transition rates.

Table 1. The experimental data and parameters of 5D_3 - 7F_6 transition of Tb^{3+} in β -NaGdF₄ NCs at various temperatures.

Temp.(K)	12	62	112	162	212	262	312	
Sample								
τ (μ s)	a	170 \pm 5.4	160 \pm 4.0	150 \pm 0.34	90 \pm 0.07	69 \pm 0.02	31 \pm 0.03	14 \pm 0.003
	b	460 \pm 0.1	455 \pm 0.1	453 \pm 0.1	375 \pm 0.1	286 \pm 0.7	82 \pm 0.1	55 \pm 0.2
	c	500 \pm 8.3	495 \pm 5.3	490 \pm 0.2	362 \pm 6.2	305 \pm 0.8	123 \pm 1.6	67 \pm 0.9
Γ (s^{-1})	a	5882	6250	6667	11111	14534	31958	71923
	b	2174	2198	2208	2667	4237	12195	18182
	c	2000	2020	2041	2762	3279	8130	14925
$I_4/(I_3+I_4)$	a	0.81	0.78	0.81	0.82	0.84	0.86	0.88
	b	0.66	0.69	0.67	0.68	0.69	0.73	0.82
	c	0.69	0.69	0.69	0.71	0.77	0.79	0.81
$\Gamma_{nr}(s^{-1})$	a	4764	4875	5400	9111	12209	27484	63292
	b	1435	1517	1479	1813	2924	8902	14909
	c	1380	1394	1408	1961	2525	6423	12089

A rare-earth ion in an excited state i decays with a lifetime τ_i given by

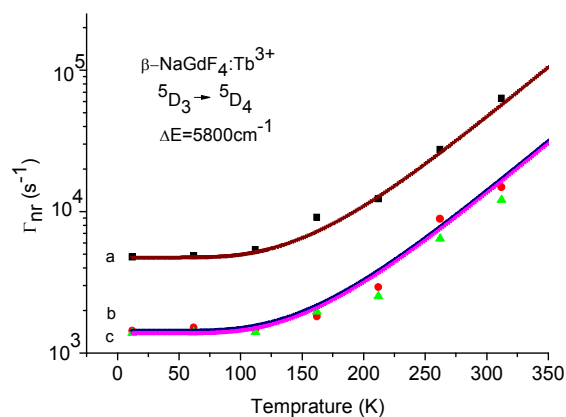


Fig. 12 Temperature dependence of MR rates of samples a (experimental data-black square, fitted curve by eq. (8) - red line); b (experimental data-red square, fitted curve by eq. (8) - blue line) and c (experimental data-green triangle, fitted curve by eq. (8) - pink line).

$$\frac{1}{\tau_i} = \sum_j (A_{ij} + W_{ij}) = \Gamma_{ir} + \Gamma_{inr}, \quad (5)$$

where A_{ij} and W_{ij} are the rates for radiative and nonradiative decays, respectively, and the summation is over all terminal states j . MR processes are sometimes dominant modes of relaxation of 4f-states. The probability of spontaneous multiphonon emission increases as the energy gap decreases. The probability also depends on the energies of phonons and the densities of their states. The excitation energy is always supplied to 5D_4 through 5D_3 in host lattices with large forbidden gap in the case of the 4f-5d band excitation. The multiphonon emission process of ${}^5D_3 \rightarrow {}^5D_4$ sometimes becomes a dominant mode of decay of the 5D_3 state. Consequently, the 5D_4 -emission owes its intensity to the ${}^5D_3 \rightarrow {}^5D_4$ relaxation rates. This rate of multiphonon emission process of ${}^5D_3 \rightarrow {}^5D_4$, Γ_{nr} is obtained using the following relation:¹²

$$\Gamma_{nr} = \Gamma({}^5D_3) \frac{I_4}{(I_3 + I_4)} \quad (6)$$

where $\Gamma(^5D_3)$ is the reciprocal of the observed fluorescence lifetime of $^5D_3 \rightarrow ^7F_1$, and I_3 and I_4 are total quantum outputs of the 5D_3 - and 5D_4 -emissions, respectively. The MR rates of $^5D_3 \rightarrow ^5D_4$ at various temperatures were derived from Eq. (5), see Table 1.

The temperature dependence of nonradiative transition rates is usually explained by the multiphonon process of a single phonon mode, as performed in Refs. 24-33. Phonons of various modes may be involved in the 5D_3 - 5D_4 relaxation. Moreover, the variation of thermal population of the levels near 5D_3 makes the temperature dependence further complicated. Thus, the 5D_3 - 5D_4 nonradiative relaxation rates caused by spontaneous multiphonon emission strongly depend on the vibrational properties of matrices.

The phonon energies covering the 5D_3 - 5D_4 energy gap ($\sim 5800 \text{ cm}^{-1}$) must be considerably large to minimize the order of the multiphonon process. Because the density of such phonons available is low at room temperature and below, the observed nonradiative transition probabilities are considered almost as those of the spontaneous multiphonon emission. If n is the smallest integer such that $n\hbar\omega_{max} \geq \Delta E = 5800 \text{ cm}^{-1}$, one assumes that

$$W(T) = W(0) [1 - \exp(-\Delta E / k_B T)]^{-n}. \quad (7)$$

Eq. (7) was used to describe the temperature dependence of MR rate.²⁵⁻²⁹ However, when the energy gap ΔE became larger, for example, $\Delta E = 5800 \text{ cm}^{-1}$, the factor $\exp(-\Delta E / k_B T) \rightarrow 0$ rapidly with temperature T from 12K to 350 K. The experiment showed that for the case of weak electron-phonon coupling multiphonon nonradiative transition probability $\Gamma_{nr}(T)$ decreased rapidly with increasing order $n = \Delta E / \hbar\omega$ of the process, or normalized energy gap. The phonon modes in the narrow range near the highest frequency (cutoff frequency) of the phonon spectrum contributed greatly to $\Gamma_{nr}(T)$, because they conserved energy in the lowest-order process.²³ As a consequence, for relaxation by emission of phonons of a single frequency ω , where $\omega \approx \omega_{max} = \omega_{co}$, the order of the process required to bridge an energy gap ΔE is $n = \Delta E / \hbar\omega$. The nanostructure dimensions eliminate the low-frequency vibrations, providing a cutoff in the phonon density-of-states that depends on particle size. The size-resonant spherical and torsional modes dominate near the cutoff. The main peak positions are 291, 356, and

401 cm⁻¹ for NaGdF₄ NCs in the micro-Raman spectra.²⁴

If the temperature is not very high and the Huang-Rhys parameter S is very small ($S \ll 1$), the temperature dependence for an n-phonon process using single-frequency model is given by³¹⁻³³

$$\Gamma_{nr}(T) = \Gamma_{nr}(0) \left[\frac{1}{\exp(\hbar\omega / k_B T) - 1} + 1 \right]^{\Delta E / \hbar\omega} \quad (8)$$

where $\Gamma_{nr}(0)$ is the spontaneous emission probability at $T = 0\text{K}$, take $\Gamma_{nr}(0) = \Gamma_{nr}(12\text{K})$, $\hbar\omega = \hbar\omega_{co} = 401 \text{ cm}^{-1}$.

Fig.12 shows that the experimental data agreed well with the theoretical curves, the temperature dependence of MR rates is described well by the model.

To avoid energy transfer and cross-relaxation processes, the doping concentration of Tb³⁺ in β -NaGdF₄ NC samples were limited to 1 mol %. Given that the nonradiative channels increase, the luminescence efficiencies reduce for the small NCs. Enlargement of the local field is considered an effective approach to enhance luminescence efficiency because the overall luminescent efficiency of the system depends on the ratio between the radiative and nonradiative lifetimes.

In conclusion, the normal modes of vibration of perfect lattice modified by the substitutional impurity (Eu³⁺) defects was investigated. These modes are not traveling plane wave as those of the perfect lattice but rather vibrational modes centered at the defects with the amplitude of vibrational exponentially attenuating with distance from the impurity. The two one-phonon PSBs resulted from the localized modes were observed. The average energy of the phonons $\hbar\omega_L$ involved in the sideband formation were derived, $\hbar\omega_{L1} = 612 \text{ cm}^{-1}$ and $\hbar\omega_{L2} = 1077 \text{ cm}^{-1}$, respectively. The intensity of PSB is Poisson-distributed $I = e^{-S} (S^n/n!)$, with S being the Huang-Rhys factor and n the number of phonon replicas. The intensity ratio of one- and two-phonon sidebands is $I_2/I_1 = S/2 \ll 1$. So only one-phonon PSB can be observed in rare earth dopant materials ($s < 1$).

The MR rates of Tb³⁺ $^5D_3 \rightarrow ^5D_4$ were determined from the emission spectra and fluorescence decays at different temperatures. The nanostructure dimensions eliminated the low-frequency vibrations, providing a cutoff in the phonon density of states that depends on particle size. The ω_{max} value of 401 cm⁻¹ was selected as the cutoff

frequency ω_{co} . In the MR of the RE ions, the phonons with $\hbar\omega_{max}$ play the important role. Because the numbers connecting the energy gap ΔE needed to emit are $N = \Delta E / \hbar\omega_{max}$. It is obvious that the N_{min} only corresponds to the phonons $\hbar\omega_{max}$. The smaller N is, the larger transition probability is. That means the transition probability is the best large for the phonons $\hbar\omega_{max}$. The experimental data agreed with the theoretical curves in the analysis for temperature dependences of the MR rates of ${}^5D_3 \rightarrow {}^5D_4$. The MR occurred predominantly through high-energy optical phonons.

■ ANOWLEDGMENT

The authors are grateful to the National Natural Science Foundation of China (NSFC) (Nos. 61077025, 10904140, 10774142 and 60308008) for support.

■ References

- 1 M. J. Weber, *Phys. Rev. B*, 1973, **8**, 54-64.
- 2 M. D. Sturge *Phys. Rev. B*, 1973, **8**, 6-14.
- 3 H. Dubost, L. Abouaf-Maguin, and F. Legay, *Phys. Rev. Lett.*, 1973, **22**, 145-148.
- 4 G. Zhang, X. Ying, L. Yao, and H. Chen, *J. Lumin.*, 1994, **59**, 315-320.
- 5 U. Happek, C. E. Muga, W. von der Osten, and A. J. Sievers, *Phys. Rev. Lett.*, 1994, **72**, 3903-3906.
- 6 M. P. Miller, and J. C. Wright, *J. Chem. Phys.*, 1979, **71**, 324-338.
- 7 K. Huang, A. Rhys, *Proc. R. Soc. London Ser.*, 1950, A **204**, 406 -426.
- 8 C. W. Struck, W. H. Fonger, *J. Lumin.* 1975, **10**, 1-30.
- 9 K. Huang, *Prog. Phys.*, (China) 1981 **1**, 31-85.
- 10 W. Y Jia, R. T. Brundage, and W. M. Yen, *Phys. Rev. B* 1983, **27**, 41-45.

- 11 Y. Tian, X. H. Qi, X. W. Wu, R. N. Hua, and B. J. Chen, *J. Phys. Chem. C* 2009, **113**, 10767–10772.
- 12 S. Neeraj, N. Kijima and A. Cheetham, *Chem. Phys. Lett.*, 2004, **387**, 2-6.
- 13 J. A. Alonso, F. Rivillas, M. J. Matinez-Lope and V. Pomjakushin, *J. Solid State Chem.*, 2004, **177**, 2470-2476.
- 14 H. Li, S. Zhang, S. Zhou, X. Cao, and Y. Zheng, *J. Phys. Chem. C*, 2009, **113**, 13115–13120.
- 15 H. Liu, R. A. Secco, N. Imanaka, G. Adachi, *Solid State Commun.*, 2002, **121**, 177-180.
- 16 S. Sumithraa, A. K. Tyagib, A. M. Umarjia, *Mater. Sci. Eng. B*, 2005, **116**, 14-18.
- 17 D. A. Woodcock, P. Lightfoot, and C. Ritter, *Journal of Solid State Chem.*, 2000, **149**, 92-98.
- 18 C. X. Liu, J. Y. Liu, and K. Dou, *J. Phys. Chem. B* 2006, **110**, 20277-20281.
- 19 G. Blasse, *Inter. Rev. in Phys. Chem.*, 1992, **11**, 71-100.
- 20 S. I. Pekar, *J. Exp. Theor. Phys. USSR* 20, 1950, 510-523.
- 21 R. H. Bartram, *J. Phys. Chem. Solids*, 1990, **51**, 641-651.
- 22 B. R Judd, *Phys. Rev.* 1962, **127**, 750-761.
- 23 C. S. Ofelt, *J. Chem. Phys.*, 1962, **37**, 511-520.
- 24 A. Riseberg, H. W. Moos, *Phys. Rev. Lett.* 1967, **19**, 1423-1425.
- 25 T. Miyakawa, D.L. Dexter, *Phys. Rev. B* 1970, **1**, 2961-2969.
- 26 K. K. Pukhov, V. P. Sakun, *Phys. Status Solidi B*, 1979, **95**, 391-402.
- 27 F. K. Fong, S.L. Naberhuis, M. M. Miller, *J. Chem. Phys.* 1972, **56**, 4020-4027.
- 28 M. J. Weber, *Phys. Rev. B*, 1973, **8**, 54-63.
- 29 L. A. Riseberg, M. J. Weber, in *Progress in Optics* (ed. E. Wolf), 1976, **14**, 89-159.
- 30 S. A. Egrov, J. L. Skinner, *J. Chem. Phys.*, 1995, **103**, 1533-1542.
- 31 Y. Orlovskii, *Phys. Rev. B* 1994, **49**, 3821-3830.
- 32 Z. Burshtein, *Opt. Engin.* 2010, **49**, 091005.

- 33 S. Kuboniwa, T. Hoshina, *J. Phys. Soc. Jpn*, 1972, **32**, 1059-1068.
- 34 M. Banski, A. Podhorodecki, J. Misiewicz, M. Afzaal, A. Abdelhadyc and P. O'Brienc, *J. Mater. Chem. C*, 2013, **1**, 801–807.